Whole-body biodistribution and the influence of body activity on brain kinetic analysis of the ^{11}C-PiB PET scan

Go Akamatsu[1] · Tomoyuki Nishio[1] · Kazuhiko Adachi[1,2] · Yasuhiko Ikari[1] · Michio Senda[1]

Abstract Dynamic ^{11}C-PiB PET imaging with kinetic analysis has been performed for accurate quantification of amyloid binding in patients with Alzheimer's disease (AD). In this study, we measured the whole-body biodistribution of ^{11}C-PiB in nine subjects. We then evaluated the effect of body activity on quantitative accuracy of brain ^{11}C-PiB three-dimensional (3D) dynamic PET. Based on clinical biodistribution data, we conducted phantom experiments to estimate the effect of body activity on quantification of the brain 3D dynamic ^{11}C-PiB PET data and the error introduced by body activity using six different PET camera models. One of the PET cameras was used to acquire ^{11}C-PiB brain 3D dynamic PET data on a patient with AD. We calculated the distribution volume ratio (DVR) in two kinetic methods using both the original human time-activity-curve (TAC) data and the TAC corrected for the error caused by body activity. In the early phase, both healthy subjects and patients with AD showed a biodistribution of ^{11}C-PiB that reflected regional blood flow. In the simulated early phase of the phantom experiments, activity outside the field of view led to a maximum 6.0% overestimation of brain activity in the vertex region. Conversely, the effect of body activity on the DVR estimate was small ($\leq$1.2%), probably because the tested kinetic methods did not rely heavily on early phase data. These results indicate that the effect of body activity on brain ^{11}C-PiB PET quantification is generally small and that it depends on the method of kinetic analysis, the region of interest, and the PET camera model used.

Keywords PET · ^{11}C-PiB · Biodistribution · Activity outside the field of view · Kinetic analysis

1 Introduction

Amyloid positron emission tomography (PET) imaging can reveal in vivo brain amyloid-β plaques, a pathological hallmark of Alzheimer's disease (AD). The ^{11}C-labeled Pittsburgh Compound B (^{11}C-PiB) is a widely used amyloid imaging agent in research [1]. Dynamic ^{11}C-PiB PET imaging with kinetic analysis has been performed for the accurate quantification of amyloid deposition [2].

On a related note, PET/computed tomography (CT) cameras with three-dimensional (3D) acquisition are commonly used in oncological whole-body (WB) PET imaging due to higher sensitivity and shorter scanning time than cameras with two-dimensional (2D) acquisition. However, 3D acquisition may be influenced by singles and random coincidence, which diminish image quality and quantitative capability [3–8]. In the brain ^{11}C-PiB dynamic scan using 3D acquisition, the injected activity is mostly distributed throughout the body, particularly in the early phase post-injection. Such activity outside the field of view (FOV) can lead to errors in the quantification of brain PET images within the FOV [9–12].

Despite this, the effect of body activity on brain ^{11}C-PiB dynamic scans has not been evaluated, because no studies have gathered detailed data on ^{11}C-PiB biodistribution in the neck, chest, and WB, with the exception of one study addressing radiation dosimetry [13].

✉ Go Akamatsu
akamatsu@fbri.org; akamatsu@kyudai.jp

1 Division of Molecular Imaging, Institute of Biomedical Research and Innovation, 2-2, Minatojima-Minamimachi, Chuo-ku, Kobe 650-0047, Japan

2 Department of Mechanical Engineering, Chubu University, 1200 Matsumoto-cho, Kasugai 487-8501, Japan

In the present study, we acquired the early phase biodistribution data of ^{11}C-PiB in various axial body areas in subjects who had been enrolled in various brain research protocols and had undergone a brain PET scan in the later phase. We then performed phantom experiments based on the actual human biodistribution data using a number of PET cameras in 3D mode. Finally, based on these phantom experiments, the effects of body activity on the quantitative capability of brain ^{11}C-PiB PET and on kinetic analysis were estimated.

2 Materials and methods

2.1 Subjects

In the present study, a total of 10 subjects were enrolled in various research protocols, each focusing primarily on the acquisition of late-phase brain ^{11}C-PiB PET images. In addition, we took advantage of the accumulation phase and set up an add-on protocol to measure sequential activity over time in each axial body segment. Approval was obtained from the ethics committee and informed consent was obtained from each subject for the primary study, the add-on protocol, and the subsequent data analysis.

The demographic profiles of the subjects and scans are summarized in Table 1 and described below. Six subjects with mild cognitive impairment (MCI) or suspected MCI (mean age 72.2 years, range 65–82 years) underwent a 2D WB or neck-to-chest dynamic scan with ^{11}C-PiB. Two healthy subjects and one patient with AD (mean age 59.9 years, range 51–64 years) underwent a 2D brain dynamic scan with ^{11}C-PiB. A tenth subject, a 63-year-old patient with AD, underwent a brain 3D dynamic ^{11}C-PiB scan using another PET camera. None of the subjects had any cardiovascular, respiratory, or renal diseases that could have influenced WB biodistribution or pharmacokinetics.

2.2 PET scanner and scan mode

We used an ECAT EXACT HR + scanner (Siemens/CTI, Knoxville, TN) in 2D mode to acquire whole-body ^{11}C-PiB biodistribution [14]. To allow quantitative measurement of each axial body area, dynamic WB, neck-to-chest, and brain PET scans were performed in 2D acquisition mode.

In the subsequent phantom study, we used six PET camera models and performed phantom scans in 3D mode. These six PET cameras were considered to be used for brain 3D dynamic ^{11}C-PiB PET scans in the Japanese Alzheimer's disease neuroimaging initiative (J-ADNI) project [15]. These 3D scans were performed in accordance with the standard PET imaging protocol detailed in the J-ADNI. Table 2 shows the PET camera specifications and scan parameters that were used in the phantom study.

The tenth subject (J) underwent a ^{11}C-PiB brain 3D dynamic scan using a Shimadzu SET-3000G/X (Table 2) to evaluate the effect of body activity on the brain PET acquired and analyzed in the standard J-ADNI protocol.

2.3 Dynamic whole-body and neck-to-chest PET scans to measure ^{11}C-PiB biodistribution

Dynamic WB PET scans were performed on three subjects (A, B, and C) to measure the biodistribution of ^{11}C-PiB from the top of the head to the mid-thigh. Dynamic neck-to-chest scans were performed on another three subjects (D, E, and F) to measure the ^{11}C-PiB biodistribution from the neck to the chest area in more detail.

A transmission scan was performed using a [68]Ge/^{68}Ga rod source before ^{11}C-PiB injection. The transmission scan protocols were as follows: 3 min/bed × 8 beds for the WB scan and 3 min/bed × 2 beds for the neck-to-chest scan. A dynamic emission scan was performed for a total period of

Table 1 Subject data and scan information

Subject	Axial scan range	Injection dose (MBq)	Scan mode	Clinical diagnosis	Brain PiB uptake read	PET scanner
A	Whole-body	548.1	2D	MCI	Positive	ECAT EXACT HR+
B	Whole-body	542.4	2D	MCI	Positive	ECAT EXACT HR+
C	Whole-body	567.0	2D	MCI	Positive	ECAT EXACT HR+
D	Neck-to-chest	541.8	2D	MCI	Negative	ECAT EXACT HR+
E	Neck-to-chest	514.1	2D	MCI	Positive	ECAT EXACT HR+
F	Neck-to-chest	542.9	2D	MCI	Positive	ECAT EXACT HR+
G	Brain	615.4	2D	HC	Negative	ECAT EXACT HR+
H	Brain	584.6	2D	HC	Negative	ECAT EXACT HR+
I	Brain	532.0	2D	AD	Positive	ECAT EXACT HR+
J	Brain	546.1	3D	AD	Positive	SET-3000G/X

AD Alzheimer's disease, *HC* healthy control, *MCI* mild cognitive impairment

Table 2 PET camera specifications and scan parameters in the phantom study

Vender	Shimadzu	GE	GE	Siemens	Siemens	Siemens
PET scanner	SET-3000 G/X	Discovery ST elite	Advance	Biograph Hi-Rez	Biograph TruePoint TrueV	ECAT ACCEL
Detector material	GSO	BGO	BGO	LSO	LSO	LSO
Axial FOV (mm)	260	157	153	162	216	162
Scan mode	3D	3D	3D	3D	3D	3D
Matrix size	128×128	128×128	128×128	168×168	168×168	128×128
Pixel size (mm)	2.0×2.0	2.0×2.0	2.0×2.0	2.0×2.0	2.0×2.0	2.0×2.0
Slice thickness (mm)	2.60	3.27	4.25	2.00	2.027	3.375
Number of slices	99	47	35	81	109	47
Attenuation correction method	^{137}Cs	CT	^{68}Ge/^{68}Ga	CT	CT	^{68}Ge/^{68}Ga
Scatter correction method	HDE	Model-based	Tail fitting (Bergstrom)	Model-based	Model-based	Model-based
Random correction method	Delayed	Singles	Delayed	Delayed	Delayed	Delayed
Reconstruction parameter	FORE +DRAMA	3D OSEM	FORE +OSEM	FORE +OSEM	3D OSEM	FORE +OSEM
Subset (filter cycle)/ iteration	(0)/4	40/2	16/6	14/4	21/4	16/6
Other		Z axis filter: standard		Trim: off	Trim: off	

about 40 min starting immediately after injection of ^{11}C-PiB. The WB emission scan protocol was as follows: 30 s/bed $\times$ 8 beds, repeated six times, starting at approximately 0, 7, 14, 21, 27, and 35 min after injection. The neck-to-chest emission scan protocol was as follows: 30 s/bed $\times$ 2 beds, five repeats, 45 s/bed $\times$ 2 beds, two repeats, 60 s/bed $\times$ 2 beds, two repeats, and 90 s/bed $\times$ 2 beds, one scan; therefore, the protocol consisted of a total of 10 repeats (starting at approximately 0, 2.25, 4.5, 6.75, 9, 12, 15.5, 19, 25, and 35 min after injection). Subsequently, a 20-min (4 frames $\times$ 300 s) emission scan of the brain was performed starting 50 min after injection to evaluate brain ^{11}C-PiB uptake. Finally, a transmission scan of the head was performed for 6 min.

The acquired WB dynamic data were reconstructed using Fourier rebinning and a filtered back projection (FBP) algorithm with a Gaussian post-filter [8-mm full-width at half-maximum (FWHM)]. In addition, to locate the regions of interest (ROIs), PET data were reconstructed using the ordered-subset expectation–maximization (OSEM) algorithm (4 iterations, 8 subsets) with a Gaussian post-filter (8-mm FWHM). Late-phase brain data (50–70 min after injection) were also reconstructed using the OSEM algorithm (4 iterations and 16 subsets) without a post-smoothing filter [12]. The brain images of 50–70 min after injection were visually interpreted and classified as either positive or negative by an expert ^{11}C-PiB PET physician in accordance with the J-ADNI criteria [16].

2.4 Dynamic brain PET scans to measure brain ^{11}C-PiB activity

The brain 2D dynamic PET scans were performed on three subjects (G, H, and I) to measure the time course of brain ^{11}C-PiB for a 90-min period after injection of ^{11}C-PiB. The 2D emission scan protocol was as follows: 15 s $\times$ 4, 30 s $\times$ 8, 60 s $\times$ 9, 180 s $\times$ 2, 300 s $\times$ 8, and 600 s $\times$ 3 for a total of 34 frames. A 15-min transmission followed. PET data were reconstructed using filtered back projection with a Gaussian post-filter (8-mm FWHM). Images of 50–70 min after injection were generated and visually interpreted in terms of brain ^{11}C-PiB uptake.

Another subject (J) underwent a brain 3D dynamic emission scan for 70 min starting immediately after injection based on the standard J-ADNI protocol (10 s $\times$ 6, 20 s $\times$ 3, 60 s $\times$ 2, 180 s $\times$ 2, and 300 s $\times$ 12 for a total of 25 frames). A 6-min transmission scan followed. PET data were reconstructed using the OSEM (4 iterations and 16 subsets) without a post-smoothing filter. Images of 50–70 min after injection were generated and visually interpreted in terms of brain ^{11}C-PiB uptake.

2.5 Phantom experiments

In the phantom experiments, we assumed a ^{11}C-PiB injection dose of 555 MBq and a 70-min dynamic scan. As shown in Fig. 1, we designed a set of phantoms simulating

the ^{11}C-PiB biodistribution in the human body; these consisted of a cylindrical phantom (16-cm diameter, 15-cm length; Itoi Factory Inc.) for the head, three saline bags (500 mL; Otsuka Pharmaceutical Co., Ltd.) for the neck, a National Electrical Manufacturers Association/International Electrotechnical Commission body phantom (without lung insert and spheres; Data Spectrum Corp.) for the chest, and a cylindrical phantom (15-cm diameter and 20-cm length; Itoi Factory Inc.) for the upper abdomen. These phantom sets entirely consisted of water; thus, other structures (e.g., bone) were not taken into account.

Table 3 shows the target radioactivity of ^{18}F that was injected into each part of the phantom set, simulating the ^{11}C-PiB biodistribution at the following three timepoints: post-injection 1–2 min (early phase; $early_{1-2}$), 10 min (early phase; $early_{10}$), and 50 min (late phase; $late_{50}$). The radioactivity in each phase was determined based on the human WB, neck-to-chest, and brain dynamic scan data (subjects A–I). The activity of the neck and chest phantoms was determined based on the mean %injected dose (%ID) values in the neck and chest using the dynamic WB and neck-to-chest data. The %ID was calculated as follows:

$$\% \ ID = \frac{\text{Tissue activity (MBq)}}{\text{Total injected dose (MBq)}}.$$

The activity of the abdominal phantom was determined based on the sum of mean %ID values in the liver, spleen, and kidney using the dynamic WB data. Data from the first WB and neck-to-chest scans were used as the $early_{1-2}$ data, and those from the second and third WB scans, and from the fifth and sixth neck-to-chest scans, were used as the $early_{10}$ data. The final WB and neck-to-chest scan data were corrected for decay and were used as the $late_{50}$ data,

because WB and neck-to-chest data were only available up to about 35 min after injection.

At first, a transmission or CT scan was performed with all the phantoms aligned, so that the head phantom was located in the center of the FOV (Fig. 1); an emission scan followed. Next, after removing the neck, chest, and upper abdomen phantoms, we performed emission scans of the head phantom without body activity. We performed these scans in three phantom conditions, simulating the activity at $early_{1-2}$, $early_{10}$, and $late_{50}$, respectively. The emission data simulating $early_{1-2}$ and $early_{10}$ were acquired in 5 min × 1 frame, and the $late_{50}$ data were acquired in 5 min × 4 frames.

2.6 Data analysis

2.6.1 Dynamic whole-body, neck-to-chest, and brain PET data

Image analysis was performed using the PMOD software ver.3.17 (PMOD Technologies Ltd., Switzerland). To analyze the dynamic WB and neck-to-chest PET data (subjects A–F), the ROIs were manually placed on the sum images of all frames over the brain, thyroid, lungs, heart, liver/gallbladder, spleen, kidneys, bladder, and intestine, as well as over the entire neck area (from the lower border of cerebellum to the lower border of the thyroid) and the entire chest area (from the lower border of thyroid to the upper border of the liver). A time-activity curve (TAC) was obtained and the %ID was calculated based on the radioactivity distribution in each organ and the injected dose.

To analyze the 2D dynamic brain PET data (subjects G–I), a whole-brain ROI was placed on the sum images of all

Fig. 1 Photograph and diagram of the phantom alignment. The head phantom was placed in the center of the axial field of view. The abdominal phantom was placed in the liver position off the midline. For the neck phantom, of the three bags, the one that was placed in the middle was filled with radioactivity
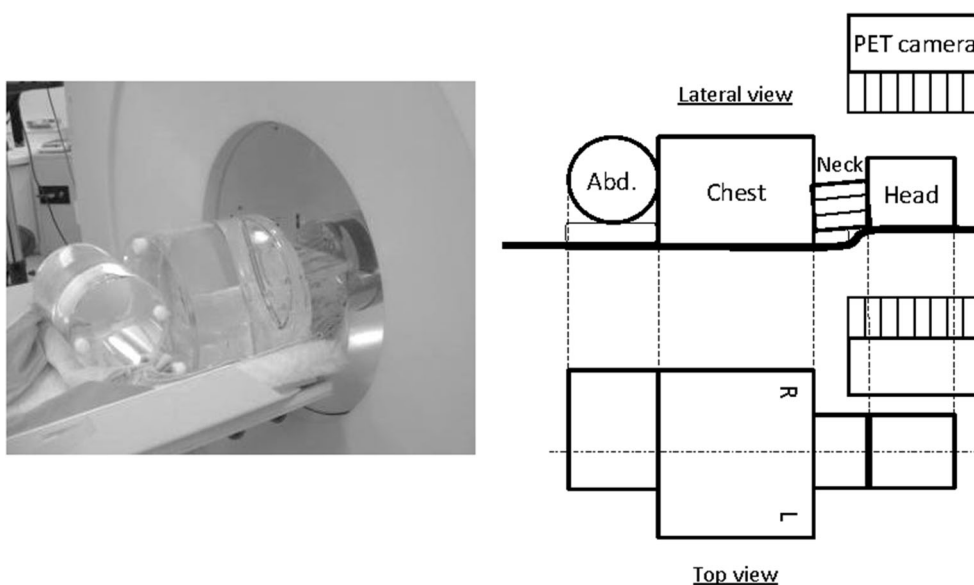
Table 3 Target activity injected into each phantom

	Head phantom (MBq)	Neck phantom (MBq)	Chest phantom (MBq)	Upper abdominal phantom (MBq)
Early$_{1-2}$	33.0	18.0	160.0	93.0
Early$_{10}$	19.0	12.0	56.0	90.0
Late$_{50}$	3.0	1.0	7.0	15.0

Actual activities were within $\pm 10\%$ of the target activities

frames. The whole-brain ROI value was then measured for each frame of the dynamic data and the %ID was calculated.

To analyze subject J, TACs were obtained using manual ROIs placed over the frontal cortex, parietal cortex, and cerebellum.

2.6.2 Phantom data with three types of activity

A 10-cm-diameter circular ROI was placed in the center of the reconstructed images of the head phantom in the early$_{1-2}$, early$_{10}$, and late$_{50}$ image data. The ROI mean value for each slice with and without body activity was obtained and compared to evaluate the effect of body activity.

2.6.3 Effect of body activity on quantitative values

Axial slices of the head phantom images were divided into three parts (caudal, middle, and cranial), each covering an axial length of about 3 cm (excluding the slices at both ends). The distance from the caudal area to the middle was about 3 cm. These three parts corresponded to the axial level of the cerebellum, frontal cortex, and parietal cortex, respectively. The estimated error (EE) was defined as the percentage difference between the head phantom ROI mean value with and without phantoms simulating body activity as follows:

TACs of the cerebellum, frontal cortex, and parietal cortex were obtained from the brain dynamic PiB-positive PET data [subject J; measured TAC (TAC$_{meas}$)]. Next, we corrected for the effect of body activity using the EE of the TAC$_{meas}$ at each timepoint, as determined using the SET-3000G/X camera. We then generated corrected TAC data (TAC$_{corr}$). We performed kinetic analysis using both TAC$_{meas}$ and TAC$_{corr}$, and then compared the distribution volume ratios (DVRs). The reference region was placed over the cerebellar cortex. Multi-linear reference tissue model 2 (MRTM2) [17] and Logan graphical analysis with reference tissue (LGAR) [18] were used in the kinetic analysis. We used the TAC data of 0–70 min to obtain the operational equation model. Subsequently, the DVRs were estimated using linear or multi-linear regression for $t > t^*$, where t^* is the equilibrium time for the regression. The LGAR requires a fit to the latter linear portion of the plot only. In contrast, the MRTM2 can include more data points, since it uses a multi-linear approach [19]. Based on these, we set t^* equal to 1650 s for LGAR and 0 s for MRTM2 (all data were used).

3 Results

3.1 Whole-body ^{11}C-PiB biodistribution

Figure 2 shows the sequential WB and neck-to-chest maximum intensity projection (MIP) images after injection of ^{11}C-PiB. Immediately after ^{11}C-PiB injection, images reflecting blood perfusion were obtained. The organ uptake was rapidly washed out, except for that in the brain, liver, intestine, and urinary tract. The biliary tracts and intestine gradually became intensely visible over time. Figure 3 shows the TACs for the whole brain, thyroid, neck, chest, liver/gallbladder, spleen, kidneys, bladder, and intestine that were obtained

$$\text{Estimated error (EE)} = \frac{\text{Mean activity with phantoms (Bq/mL)} - \text{mean activity without phantoms (Bq/mL)}}{\text{Mean activity without phantoms (Bq/mL)}}.$$

The EE was calculated in each slice of the brain phantom and averaged to evaluate the effect of body activity on the brain. All scan frames belonging to the late$_{50}$ phase of the phantom experiments were averaged to reduce the effect of image noise. The EE at any timepoint was estimated by linear interpolation of the EE at the measured three timepoints.

from the dynamic WB, neck-to-chest, and brain data. Whole-brain uptake of ^{11}C-PiB reached a maximum about 2 min after injection. Uptake by the thyroid, chest, spleen, and kidneys was at its highest in the first frame of the dynamic data. Conversely, uptake by the liver, bladder, and intestine gradually increased over time up to 35 min after injection.
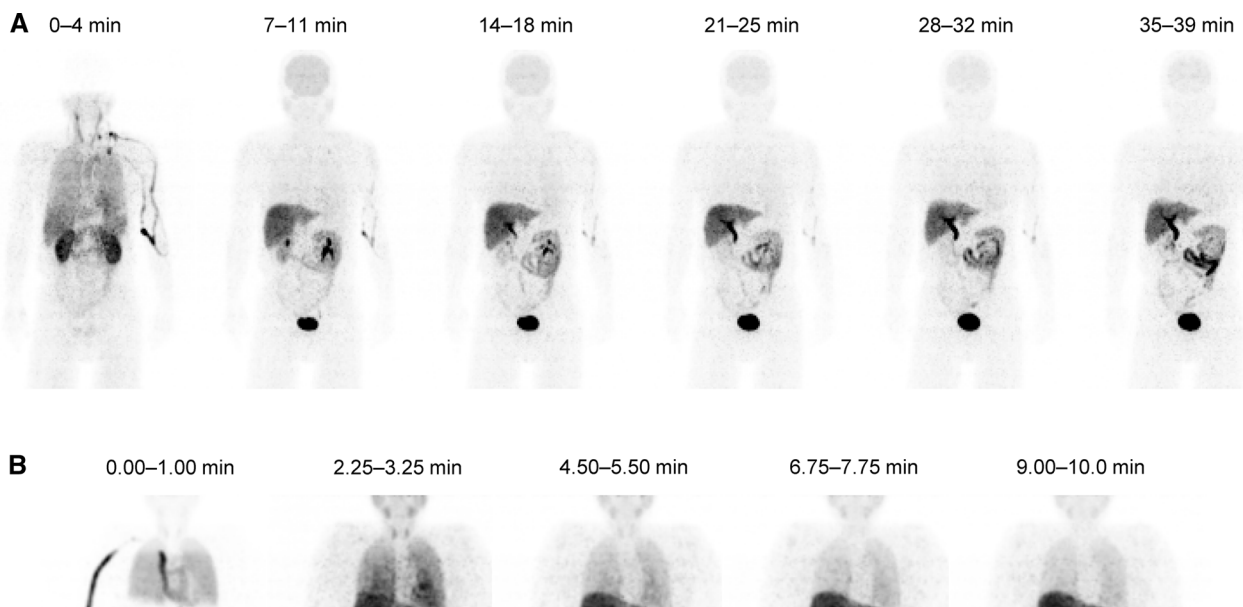
Fig. 2 Serial whole-body (WB) maximum intensity projection (MIP) images after ^{11}C-PiB injection. A WB MIP image from the head to femoral region in subject B (**a**). Neck-to-chest MIP image in subject E (**b**)
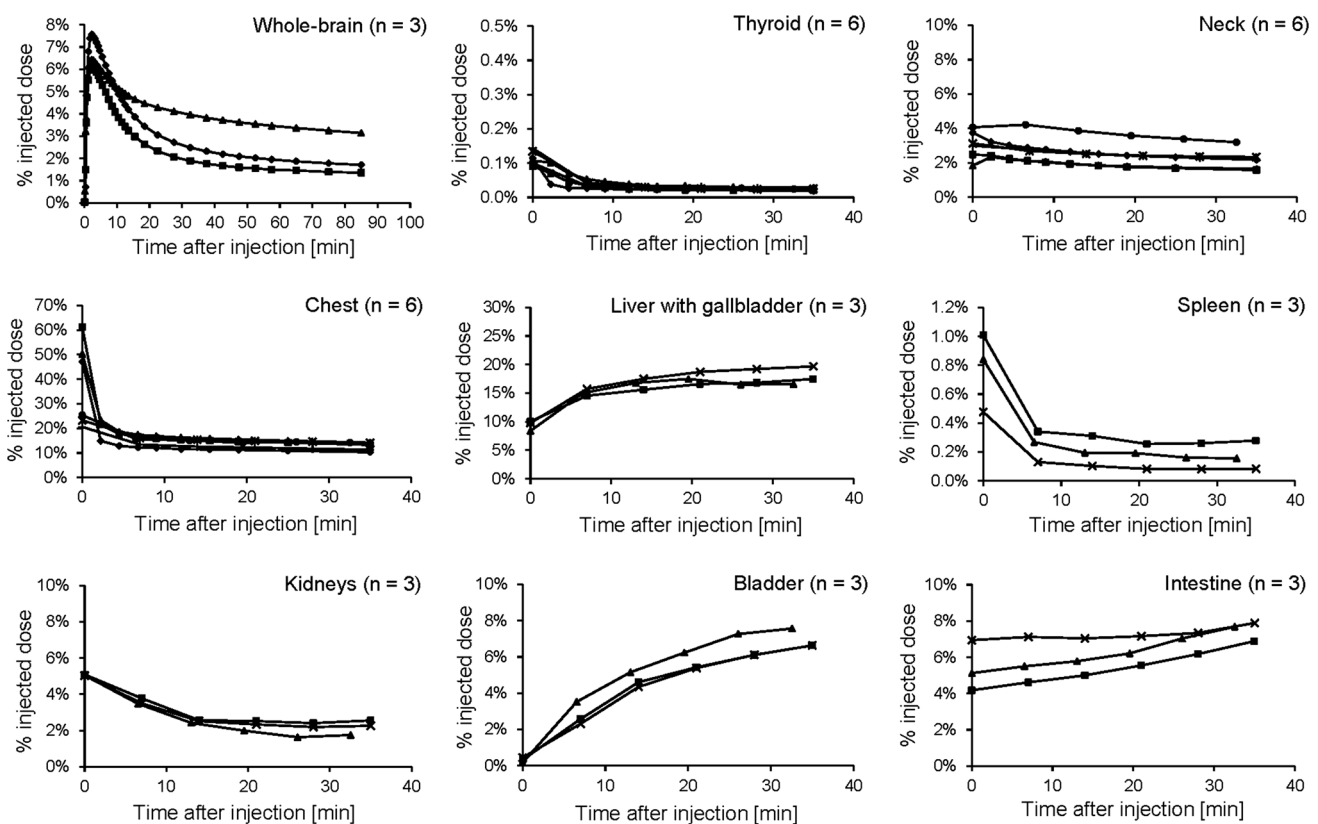

Fig. 3 Time-activity curves (TACs) for each organ (whole-brain, thyroid, neck, chest, liver/gallbladder, spleen, kidneys, bladder, and intestine). Each line indicates single-subject data. The whole-brain TAC was calculated from the dynamic brain scan. The other TACs were calculated from the dynamic whole-body and neck-to-chest scans

3.2 Phantom experiments

Table 3 shows the radioactivity injected into each phantom, determined based on the dynamic human PET scan data. Figures 4, 5, 6 show the relative ROI value at each slice level of the head phantom image with and without the phantoms simulating body activity for the three phases of post-injection. The EE calculated from the phantom experiments is also shown in Table 4. The ROI value at each slice level was generally constant without the body activity for using each PET camera and during all phases. However, using the ECAT ACCEL, an underestimation of 3.7% was observed at the caudal level during the early$_{1-2}$ phase. Conversely, using the SET-3000G/X, there was a maximum 6.0% overestimation at the cranial level. The differences in the values measured in ROIs with or without body activity were relatively small during the late$_{50}$ phase (Fig. 6).

3.3 Effect of body activity on kinetic analysis

Figure 7 shows TAC$_{meas}$ and TAC$_{corr}$ in the cerebellum, frontal cortex, and parietal cortex of subject J. The TAC$_{corr}$ values were lower than the TAC$_{meas}$ values. The DVR calculated using TAC$_{corr}$ in the frontal and parietal cortexes was slightly lower than that calculated using TAC$_{meas}$. The percentage differences in the frontal and parietal cortexes calculated using MRTM2 were −0.9 and 0.0%, respectively, and those calculated using LGAR were 0.0 and −1.2%, respectively.

4 Discussion

In the present study, we measured the sequential whole-body biodistribution of ^{11}C-PiB over time. We also estimated the effect of body activity on the quantified values of

Fig. 4 Plots of the head phantom region of interest values in the head at each slice level; the values without body activity are used as a baseline. The graphs show changes with and without body activity at simulated 1–2 min after injection (early$_{1-2}$). The PET camera models used were the SET-3000G/X (**a**), Discovery ST Elite (**b**), Advance (**c**), Biograph Hi-Rez (**d**), Biograph TruePoint TrueV (**e**), and ECAT ACCEL (**f**). In the caudal, middle, and cranial areas, the EE was calculated
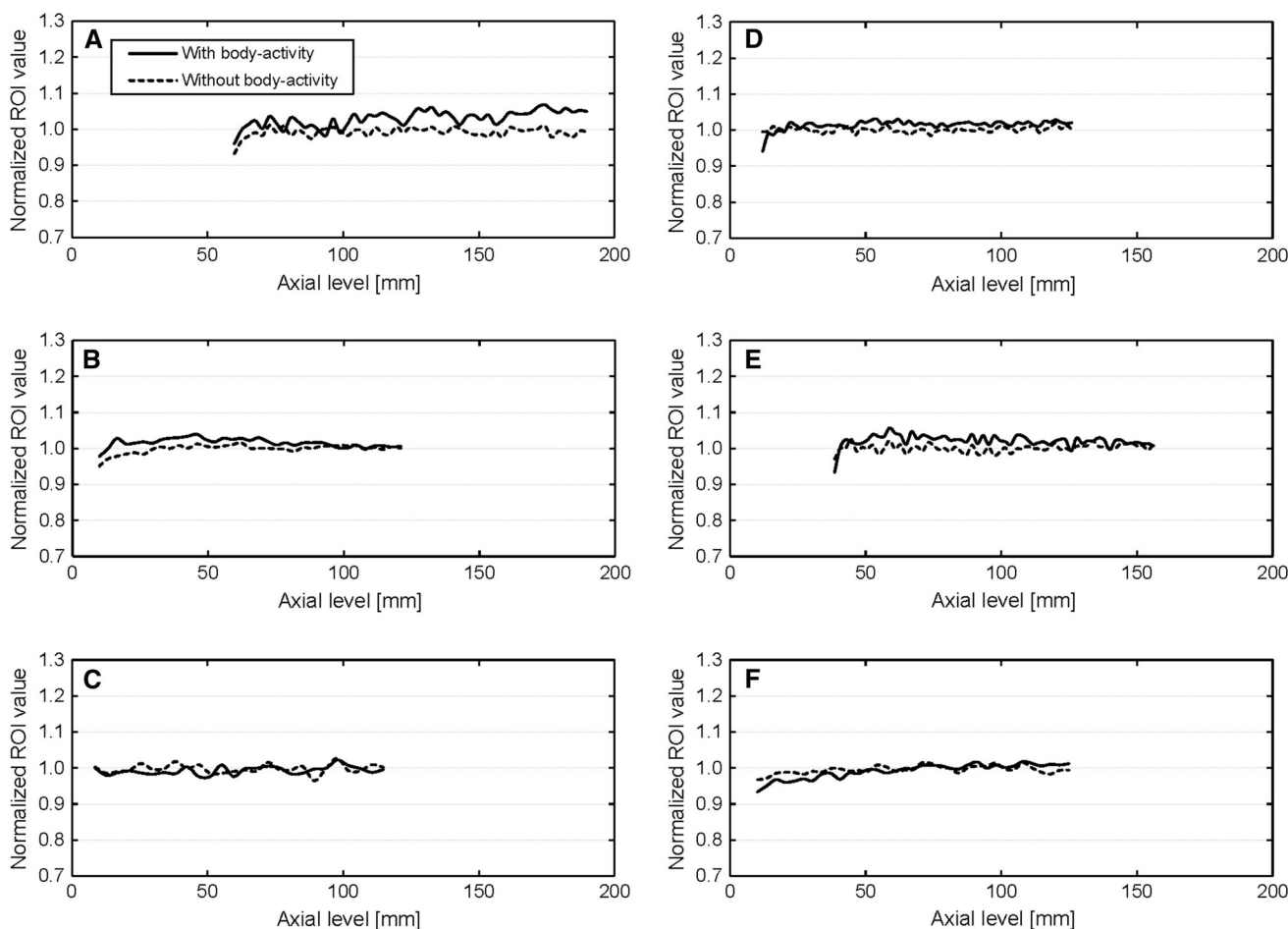
Fig. 5 Plots of the head phantom relative values measured in regions of interest at each slice position with or without body activity at simulated 10 min after injection (early$_{10}$). The PET camera models used were the SET-3000G/X (**a**), Discovery ST Elite (**b**), Advance (**c**), Biograph Hi-Rez (**d**), Biograph TruePoint TrueV (**e**), and ECAT ACCEL (**f**)

the brain ^{11}C-PiB PET based on self-designed phantom experiments using a number of PET camera models. We found that body activity had only a small effect on measured brain activity, with exceptions in the cases of a few PET cameras in the early post-injection phase. We also found that the error of the estimated DVR value was relatively small ($\leq 1.2\%$) when using one such camera (SET-3000G/X scanner) based on the kinetic methods tested in this study (MRTM2 and LGAR).

Sequential WB images of ^{11}C-PiB distribution showed activity in the heart and lungs, in a blood pool in the neck and chest area, and in the kidney and intestine, for about 10 min after injection (Fig. 2). There was high consistency among subjects, irrespective of whether they were positive or negative for late-phase brain amyloid deposition. In the early phase, uptake by the lungs, liver, and blood in the neck and chest was much higher than in the brain. Uptake in the neck and chest decreased by 20 min after injection and fell further in the later phase. In contrast, uptake in the bladder and intestine gradually increased. These results

were consistent with a previous dosimetry study [13]. Because activity in the neck-to-chest area is considered the main source of error in brain quantitation, late-phase images, which are routinely used for visual interpretation and standardized uptake value ratio (SUVR) measurement, are minimally affected by the body activity.

Using self-designed phantom experiments that were based on the measured human whole-body distribution of ^{11}C-PiB, we estimated the error caused by the body activity at each axial level of the brain using various PET cameras. We also evaluated the effect of such activity on kinetic analysis using the SET-3000G/X camera. The results showed that body activity caused non-uniform errors that depended on the axial localization within the brain and on the PET camera model. This result corroborated the previous studies [10, 12]. When radioactivity exists outside the FOV, single gamma rays from outside the FOV can be detected, especially at the far end of the axial FOV. This radiation increases singles and random coincidence, and they might influence brain PET camera uniformity, as
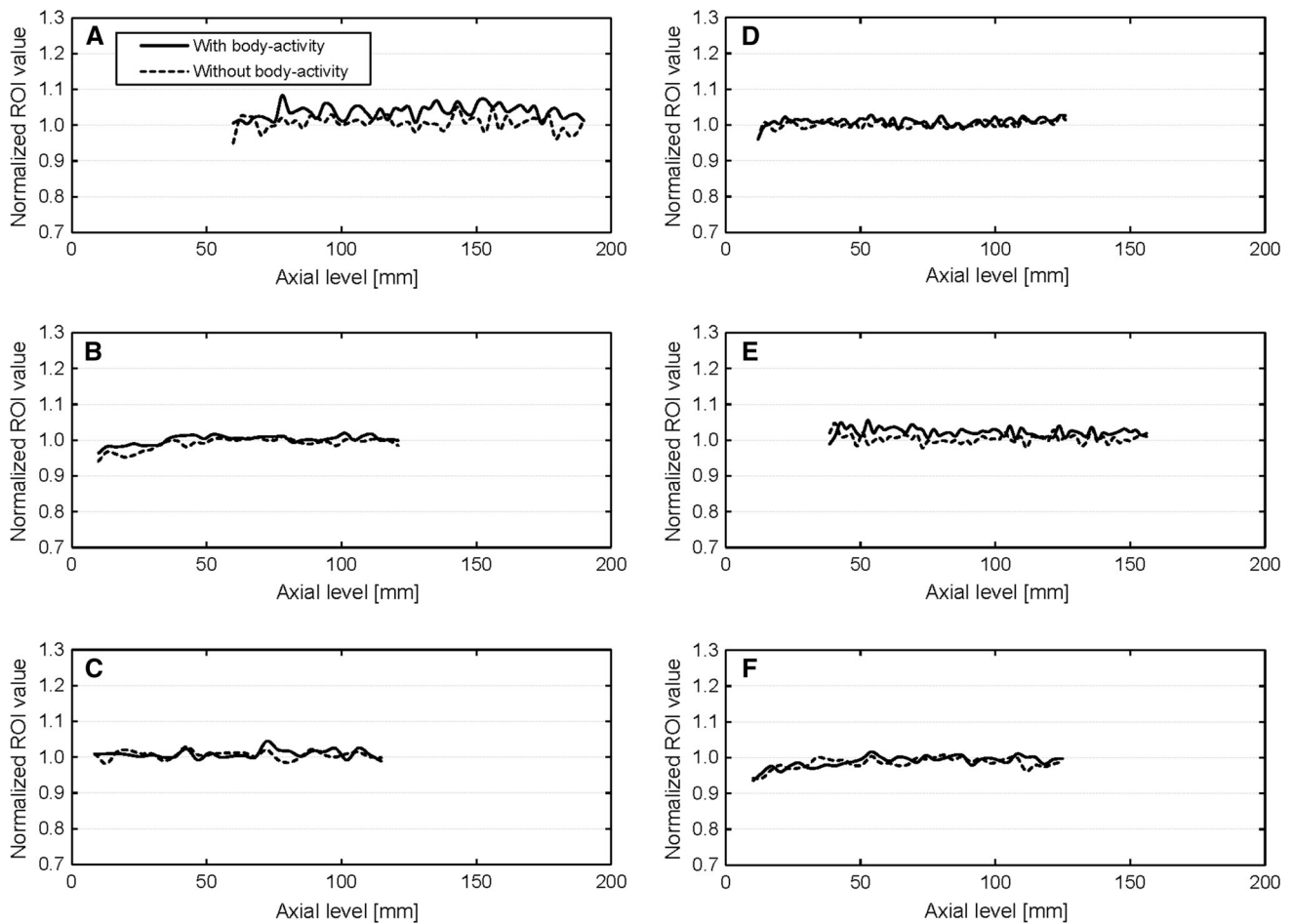
Fig. 6 Plots of the head phantom relative values measured in regions of interest at each slice position with or without body activity at simulated 50 min after injection (late$_{50}$). The PET camera models used were the SET-3000G/X (**a**), the Discovery ST Elite (**b**), Advance (**c**), Biograph Hi-Rez (**d**), Biograph TruePoint TrueV (**e**), and ECAT ACCEL (**f**)

Table 4 Estimated error (EE) calculated from the phantom data

Scan phase	Axial level	SET-3000 G/X (%)	Discovery ST elite (%)	Advance (%)	Biograph Hi-Rez (%)	Biograph TruePoint TrueV (%)	ECAT ACCEL (%)
Early$_{1-2}$	Caudal	+1.5	−1.1	−1.2	−1.3	+1.6	−3.7
	Middle	+3.8	−1.2	−0.1	+3.4	+2.3	−0.8
	Cranial	+6.0	−1.8	−0.1	+3.0	+1.1	+1.0
Early$_{10}$	Caudal	+2.5	+2.9	−0.9	−2.2	+1.2	−2.1
	Middle	+4.4	+1.7	−0.5	+1.8	+2.3	+0.2
	Cranial	+3.9	+0.1	+0.3	+1.3	+1.0	+1.1
Late$_{50}$	Caudal	+2.4	+2.1	0.0	+1.7	+0.8	−0.4
	Middle	+3.4	+0.4	+0.9	+0.6	+1.4	0.0
	Cranial	+3.6	+1.0	+0.2	+0.8	+1.7	+1.2

shown in Fig. 4 [5, 10, 12]. It should be noted that an end shield may be available that can be attached to the gantry [9]. This would be effective in blocking those gamma rays from the body. However, such a shield was not used in the present study.

Furthermore, in the present study, the quantitative value of DVR was scarcely affected by the body activity. Specifically, the effect of body activity on the DVR estimate was small, because the kinetic analyses performed in this study did not rely heavily on early phase data, which
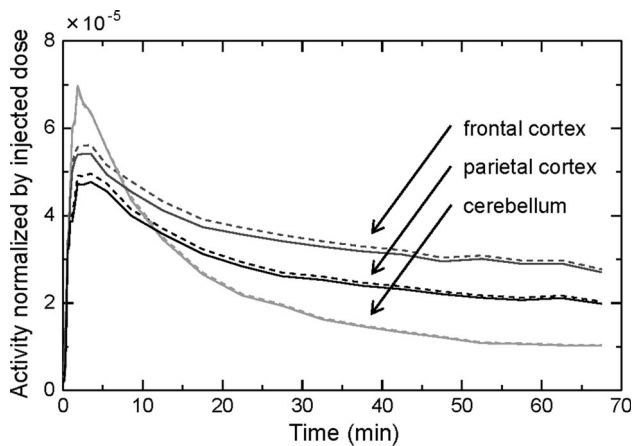
Fig. 7 Time-activity curves (TACs) for the frontal cortex, parietal cortex, and cerebellum, obtained using brain a three-dimensional dynamic scan with an SET-3000G/X camera in a patient with Alzheimer's disease. The vertical axis indicates activity (Bq/mL) normalized by the injected activity (MBq). The broken lines are the measured TACs (TAC$_{meas}$). The solid lines are the TACs corrected for the effect of body activity using EE obtained from the phantom experiments (TAC$_{corr}$)

were more influenced by body activity in a non-uniform way. If we use the smaller $t*$ timepoint for the LGAR model, or if we use other kinetic models [2, 19–21], body activity may influence the quantified estimates derived by the kinetic analysis. Conversely, simple ratio quantification, such as SUVR, is considered robust for body activity, because it does not use the early phase data. However, the activity outside the FOV may influence image noise level, although we did not evaluate the effect of body activity on the image noise. Therefore, a further study is required to examine the effect of activity outside the FOV on the voxel-based analysis, because it is sensitive to the image noise level.

In the results of the present study, the influence of body activity on the quantitative accuracy of ^{11}C-PiB PET was generally small when we did not use much early phase data. Conversely, several previous studies have reported that an external shield is useful in eliminating the effect of body activity [9, 10, 12, 22–24]. However, this carries an additional cost and may potentially limit the flexibility of subject positioning.

5 Conclusion

We measured the serial, whole-body biodistribution of ^{11}C-PiB in detail. In addition, we evaluated the effect of body activity on brain ^{11}C-PiB PET quantification and kinetic analysis. Our results indicate that the effect of body activity on the quantitative capabilities of brain ^{11}C-PiB PET is generally small and that it depends on the method of

quantitative analysis, the location of the axial FOV, and the PET camera model. Therefore, when using early phase PET data from the brain, it may be prudent to evaluate the effect of activity outside the FOV using appropriate phantoms beforehand.

References

1. Klunk WE, Engler H, Nordberg A, Wang Y, Blomqvist G, Holt DP, et al. Imaging Brain Amyloid in Alzheimer's Disease with Pittsburgh Compound-B. Ann Neurol. 2004;55:306–19.
2. Price JC, Klunk WE, Lopresti BJ, Lu X, Hoge JA, Ziolko SK, et al. Kinetic modeling of amyloid binding in humans using PET imaging and Pittsburgh Compound-B. J Cereb Blood Flow Metab. 2005;25:1528–47.
3. Sossi V, Barney JS, Harrison R, Ruth TJ. Effect of scatter from radioactivity outside of the field of view in 3D PET. IEEE Trans Nucl Sci. 1995;42:1157–61.
4. Spinks TJ, Miller MP, Bailey DL, Bloomfield PM, Livieratos L, Jones T. The effect of activity outside the direct field of view in a 3D-only whole-body positron tomograph. Phys Med Biol. 1998;43:895–904.
5. Ferreira NC, Trebossen R, Bendriem B. Assessment of 3-D PET quantitation: influence of out of the field of view radioactive sources and of attenuating media. IEEE Trans Nucl Sci. 1998;45:1670–5.
6. Matheoud R, Secco C, Della Monica P, Leva L, Sacchetti G, Inglese E, et al. The effect of activity outside the field of view on image quality for a 3D LSO-based whole body PET/CT scanner. Phys Med Biol. 2009;54:5861–72.
7. Tarantola G, Zito F, Gerundini P. PET instrumentation and reconstruction algorithms in whole-body applications. J Nucl Med. 2003;44:756–69.
8. Votaw JR, White M. Comparison of 2-dimensional and 3-dimensional cardiac 82Rb PET studies. J Nucl Med. 2001;42:701–6.
9. Thompson CJ, Moreno-Cantu JJ. Measurement of the change in noise-effective count rate during PET brain studies with additional shielding. IEEE Trans Nucl Sci. 2002;49:2057–61.
10. Hasegawa T, Suzuki M, Murayama H, Irie T, Fukushi K, Wada Y. Influence of radioactivity out of the field of view on 3D PET

dynamic measurement with [11C]MP4A. IEEE Trans Nucl Sci. 1999;46:1087–92.

11. Iida H, Miura S, Shoji Y, Ogawa T, Kado H, Narita Y, et al. Noninvasive quantitation of cerebral blood flow using oxygen-15-water and a dual-PET system. J Nucl Med. 1998;39:1789–98.

12. Mawlawi O, Van Heertum R, Laruelle M. The effect of activity from outside the field of view on accurate quantification of 3D PET images. Brain Imaging Using PET. 2002 :9–14.

13. Scheinin NM, Tolvanen TK, Wilson IA, Arponen EM, Någren KA, Rinne JO. Biodistribution and radiation dosimetry of the amyloid imaging agent 11C-PIB in humans. J Nucl Med. 2007;48:128–33.

14. Brix G, Zaers J, Adam LE, Bellemann ME, Ostertag H, Trojan H, et al. Performance evaluation of a whole-body PET scanner using the NEMA protocol. National electrical manufacturers association. J Nucl Med. 1997;38:1614–23.

15. Iwatsubo T. Japanese Alzheimer's disease neuroimaging initiative: present status and future. Alzheimers Dement. 2010;6:297–9.

16. Yamane T, Ishii K, Sakata M, Ikari Y, Nishio T, Ishii K, et al. Inter-rater variability of visual interpretation and comparison with quantitative evaluation of (11)C-PiB PET amyloid images of the Japanese Alzheimer's disease neuroimaging initiative (J-ADNI) multicenter study. Eur J Nucl Med Mol Imaging. 2017;44:850–7.

17. Ichise M, Liow JS, Lu JQ, Takano A, Model K, Toyama H, et al. Linearized reference tissue parametric imaging methods: application to [11C]DASB positron emission tomography studies of the serotonin transporter in human brain. J Cereb Blood Flow Metab. 2003;23:1096–112.

18. Logan J, Fowler JS, Volkow ND, Wang GJ, Ding YS, Alexoff DL. Distribution volume ratios without blood sampling from graphical analysis of PET data. J Cereb Blood Flow Metab. 1996;16:834–40.

19. Yaqub M, Tolboom N, Boellaard R, van Berckel BNM, van Tilburg EW, Luurtsema G, et al. Simplified parametric methods for [11C]PIB studies. Neuroimage. 2008;42:76–86.

20. Zhou Y, Ye W, Brasić JR, Crabb AH, Hilton J, Wong DF. A consistent and efficient graphical analysis method to improve the quantification of reversible tracer binding in radioligand receptor dynamic PET studies. Neuroimage. 2009;44:661–70.

21. Zhou Y, Resnick SM, Ye W, Fan H, Holt DP, Klunk WE, et al. Using a reference tissue model with spatial constraint to quantify [11C]Pittsburgh compound B PET for early diagnosis of Alzheimer's disease. Neuroimage. 2007;36:298–312.

22. Hasegawa T, Michei C, Kawashima K, Murayama H, Nakajima T, Matsuura H, et al. A study of external end-shields for PET. IEEE Trans Nucl Sci. 2000;47:1099–103.

23. Thompson CJ, Kecani S, Boelen S. Evaluation of a neck shield for use during neurological studies with a whole-body PET scanner. IEEE Trans Nucl Sci. 2001;48:1512–7.

24. Ibaraki M, Sugawara S, Nakamura K, Kinoshita F, Kinoshita T. The effect of activity outside the field-of-view on image signal-to-noise ratio for 3D PET with (15)O. Phys Med Biol. 2011;56:3061–72.